Supporting Information

Synergistic cation/anion modulation of metal phosphorus trichalcogenides for enhanced potassium-ion storage performance

Xiao-Hui Wu[1, #, *], *Li-Bing Yang*[1, #], *Ming-Jun Zhao*[1], *Mu-Rong Xu*[1], *Wei-Jun Jiang*[1], *Bing-Jie Feng*[1], *Jia-Jie Liu*[1], *and Yi Zhao*[1, *]

[1] College of Chemistry and Materials Science, Fujian Provincial Key Laboratory of Advanced Materials Oriented Chemical Engineering, Strait Institute of Flexible Electronics (SIFE, Future Technologies), Fujian Normal University, Fuzhou 350117, China

E-mail: sherrywu@fjnu.edu.cn, ifeyzhao@fjnu.edu.cn

1. Experimental section

1.1 Materials

Ferric oxide powder (AR) and sulfur powder (CP) were purchased from Sinopharm. Cobalt (II) oxide powder (AR) was purchased from Guangfu. Nickel (II) oxide powder (99.5%) was purchased from Macklin. Magnesium oxide powder (>97%), zinc oxide powder (>99%), selenium powder (99.99%), N-methyl-2-pyrrolidone (NMP) (>99%) and perylene-3,4,9,10-tetracarboxylic dianhydride (PTCDA, 98%) were purchased from Adamas. Porous carbon was purchased from Aladdin. Red phosphorus powder was purchased from Acros. Ketjen black (KB), carboxy methyl cellulose sodium (NaCMC, 99%), carbon nanotubes (CNT, AR) and Super-P were obtained from Canrd. Poly (vinylidene difluoride) (PVDF, 99.5%) was purchased from SOLVAY. All chemicals were used as received without purification, unless otherwise specified.

1.2 Synthesis of ME-S@C, ME-Se@C, and ME-SSe@C

MgO, Fe_2O_3, CoO, NiO, and ZnO powers were measured in a molar mass ratio of 1: 0.5: 1: 1: 1 and homogeneously mixed by ball milling for 1 hour to form a precursor blend. This blend was calculated in air at 1200 ^{o}C for a duration of 2 hours to yield the product, hereinafter referred to as MEO. Subsequently, an equivalent mass of porous carbon was combined with MEO and dispersed in ethanol. The mixture underwent ultrasonication for 30 minutes, followed by centrifugation to separate and take the lower precipitate. The lower precipitate was then vacuum-dried at 80°C for 1 hour, resulting in the precursor MEO@C.

To synthesize the target compounds, MEO@C was mixed with phosphorus (P) and sulfur (S) or selenium (Se) in a molar ratio of 1: 1: 3. After thorough mixing, the resultant mixture was sealed within a vacuum-sealed quartz tube. The vacuum-sealed quartz tube was placed in a dual-zone tubular furnace for reaction, and the feed mixture was at the end of the quartz tube. The heating program was set as a heating rate of 10°C/min. The end of tube with sample: heating at 450°C for 60 minutes; The top of tube without sample: temperature synchronously increased to 350°C in 42 minutes and held for 60 minutes. After the heating reaction, the tube cooled with 5°C/min to come down to room temperature. The samples were subjected to a purification process using carbon disulfide (CS_2) for three cycles, and then by using chloroform ($CHCl_3$) for three cycles, followed by drying under vacuum conditions at 80°C for 12 hours. Finally, the ME-SSe@C product can be obtained. This process yielded the samples of $MEPS_3$@C (ME-S@C), $MEPSe_3$@C (ME-Se@C), and $MEPS_{1.4}Se_{1.6}$@C (ME-SSe@C).

1.3 Synthesis of ME-S@C/CNT, ME-Se@C/CNT, and ME-SSe@C/CNT

With the weight of ME-SSe@C fixed, ME-SSe@C and carbon nanotubes were mixed with various mass ratios of 3: 1, 1.5: 1, and 1: 1. The mixtures were placed in the ball mill pot for ball milling. The ball/powder ratio was 100: 1, and the total ball milling time was 40 h. To prevent oxidation of the samples due to the high energy input, the ball milling process was intermittently halted at regular intervals. The product with a mass ratio of 1.5: 1 was named as ME-S@C/CNT, ME-Se@C/CNT, ME-SSe@C/CNT, and the rest are indicated in proportion after their names.

1.4 Preparation of anodes

The as-synthesized composite was mixed with KB and PVDF in a mass ratio of 8:1:1 and dispersed uniformly in an appropriate volume of N-methyl-2-pyrrolidone (NMP) solution. The mixture was subjected to vigorous stirring for a period of 4 hours to ensure a homogeneous slurry. Subsequently, the slurry was applied onto copper foil and vacuum-dried at 80°C overnight to achieve a uniform coating.

1.5 Preparation of PTCDA cathode

The PTCDA anode was formulated by blending 80 wt% of annealed PTCDA with 10 wt% Super-P and 10 wt% carboxymethyl cellulose (CMC). The mixture was triturated with deionized water to form a homogeneous slurry, which was then uniformly cast onto an aluminum foil serving as the current collector. The coated foil was subjected to vacuum drying at 80°C for a duration of 12 hours to ensure complete removal of solvents. Subsequently, the dried electrodes were precision-cut into aluminum disks with a diameter of 12 mm. The mass ratio of the cathode to anode active materials was meticulously maintained at approximately 6: 1 to optimize the electrochemical performance of the cell.

2. Electrochemical measurement

Standard CR2032-type coin cells were meticulously assembled within an argon-filled glove box, where the levels of oxygen and water were maintained below 0.01 ppm to ensure an inert atmosphere. For the construction of half cells of PIBs, the fabricated electrodes served as the working electrodes, with potassium foil acting as the reference electrode, Whatman GF/D glass fiber as the separator, and a 1.0 M KFSI solution in a 1: 1 volume mixture of ethylene carbonate (EC) and diethyl carbonate (DEC) as the electrolyte. In the configuration of full cells of PIBs, the aforementioned electrodes were employed as the anodes, while PTCDA electrodes were utilized as the cathodes. For the assembly of half cells of LIBs, the ME-SSe@C/CNT electrode served as the working electrode, with lithium foil acting as the reference electrode, polypropylene as the separator, and a 1 M $LiPF_6$ in DEC: DMC: EC (1: 1: 1Vol%) with 5%FEC as the electrolyte. For the assembly of half cells of SIBs, the ME-SSe@C/CNT electrode served as the working electrode, with sodium foil acting as the reference electrode, Whatman GF/D glass fiber as the separator, and 1 M NaFSI in DMC：EC：EMC (1: 1: 1 Vol%) as the electrolyte. Galvanostatic tests for both half and full cells were executed using a LAND battery-testing instrument over the voltage range of 0.005-2.8 V versus K/K^+ and 0.5-3.4 V versus K/K^+, respectively. PTCDA cathodes is activated five cycles at 0.1 A/g. Cyclic voltammetry (CV), galvanostatic intermittent titration technique (GITT) and electrochemical impedance spectroscopy (EIS) measurements were performed using an electrochemical workstation (CHI660D) within the voltage range of 0.05-2.8 V.

The GITT profiles of these two electrodes were tested under current pulse of 50 mA/g for 0.5 h and relaxation of 2 h at each interval. The potassium-ion diffusion coefficients (D_K) are calculated using the following equation:[1] $D\mathrm{K} = \frac{4}{\pi\tau}\left(\frac{m_B V_M}{M_B S}\right)^2\left(\frac{\Delta E_s}{\Delta E_\tau}\right)^2$, τ: the pulse time (1800 s); m_B: the mass of electroactive materials; V_M: the molar volume of the electroactive material; M_B: the molar mass of the electroactive material; S: the geometric area of the electrode (1.13 cm^2); ΔE_s: the potential difference caused by one pulse (the change in the steady-state voltage); ΔE_τ: the potential difference caused by constant current charge/discharge (the potential difference during each impulse).

3. Materials characterizations

The compositional analysis of the samples was conducted utilizing powder X-ray diffraction (XRD) with a diffractometer employing Cu Kα radiation (λ=1.5418 Å) (Rigaku). To delve deeper into the structural characteristics of MPX_3, a Raman spectrometer with an excitation laser beam wavelength of 633 nm from Horiba-JY T64000 was employed. The morphological examination of the synthesized samples was performed using scanning electron microscopy (SEM, Hitachi SU8100), complemented by an energy-dispersive X-ray spectroscopy detector for elemental analysis. For a comprehensive structural analysis, including morphology, crystal lattice spacing, and selected-area electron diffraction, transmission electron microscopy (TEM, JEOL JEM-F200) was deployed. The oxidation states of the samples were probed through high-resolution X-ray photoelectron spectrometry (XPS, Thermo ESCALAB 250XI).

4. Theoretical calculations

The density functional theory (DFT) calculations were performed using the Martials Studio. The Fe-Se and Mg-Se models were modeled with a 1 × 1 × 1 unit cell of $FePSe_3$ and $MgPSe_3$, respectively. The fully occupation of Mg atoms in such a Mg-Se model were replaced with Fe(0.2)/Co(0.15)/Ni(0.15)/Zn(0.1) atoms as a simplified model for ME-Se. Furthermore, a part of Se atoms in such a ME-Se model was replaced with S atoms as ME-SSe model. The geometry optimization process of four models employed the Perdew-Burke-Eznerhof (PBE) with generalized gradient approximation (GGA) for the exchange-correlation functional.[2] The basis-set was double numerical orbital base group and orbital polarization function (DNP) and the basis file was set to be 3.5. The Grimme scheme was included for the dispersion correction.[3] During the coordinate's relaxation, the convergence criteria for the geometry optimization were set to 2.0×10^{-5} Ha for energy, 0.004 Ha $Å^{-1}$ for force, and 0.005 Å for displacement. The self-consistent field convergence for the single point energy calculation was set to 1.0×10^{-5} Ha, and global orbital cutoff is 5.2 Å. The Monkhorst-Pack k-point mesh was 2 × 2 × 2.

The diffusion barriers for K^+ migration along the same path on the Mg-Se, Fe-Se, ME-Se and ME-SSe models were calculated by the transition state (TS) module in the $Dmol^3$ code.

The Grimme scheme was included for the dispersion correction.[3] The Perdew-Burke-Eznerhof (PBE) with generalized gradient approximation (GGA) was employed for the exchange-correlation functional. The basis-set was double numerical orbital base group and orbital polarization function (DNP) and the basis file was set to be 3.5. During the coordinate's relaxation, the convergence criteria for the geometry optimization were set to 2.0×10^{-5} Ha for energy, 0.004 Ha $Å^{-1}$ for force, and 0.005 Å for displacement. The self-consistent field convergence for the single point energy calculation was set to 1.0×10^{-5} Ha, and the global orbital cutoff is 4.9 Å. The Monkhorst-Pack k-point mesh was 4 × 2 × 1.

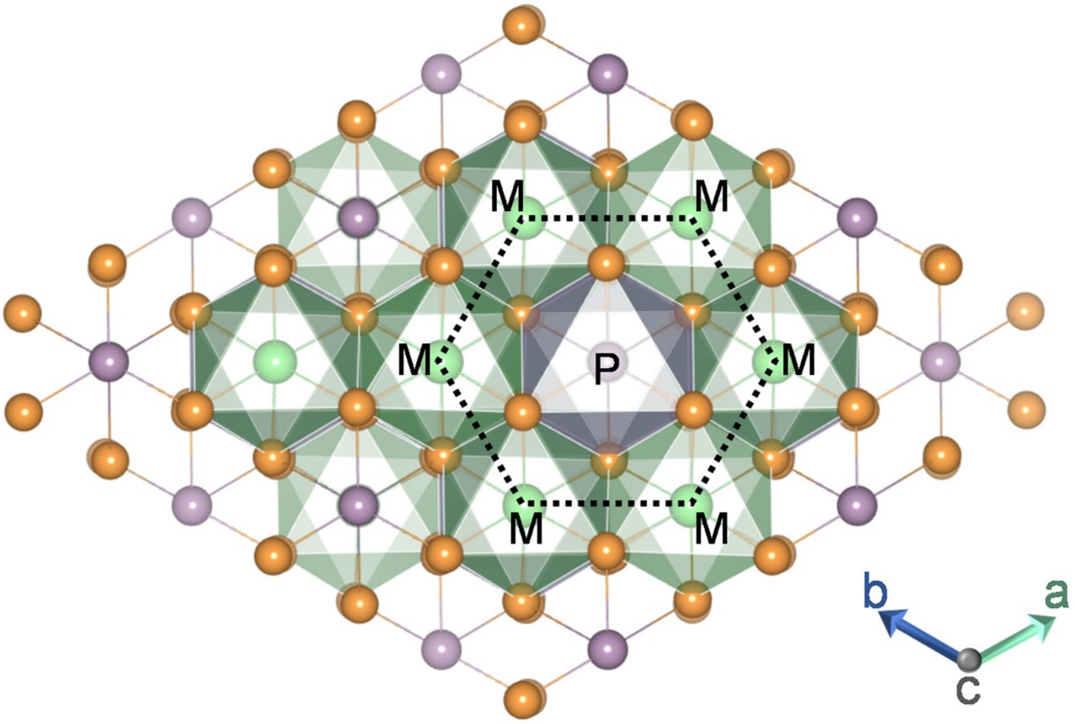

Fig. S1. The top view of MPX_3.

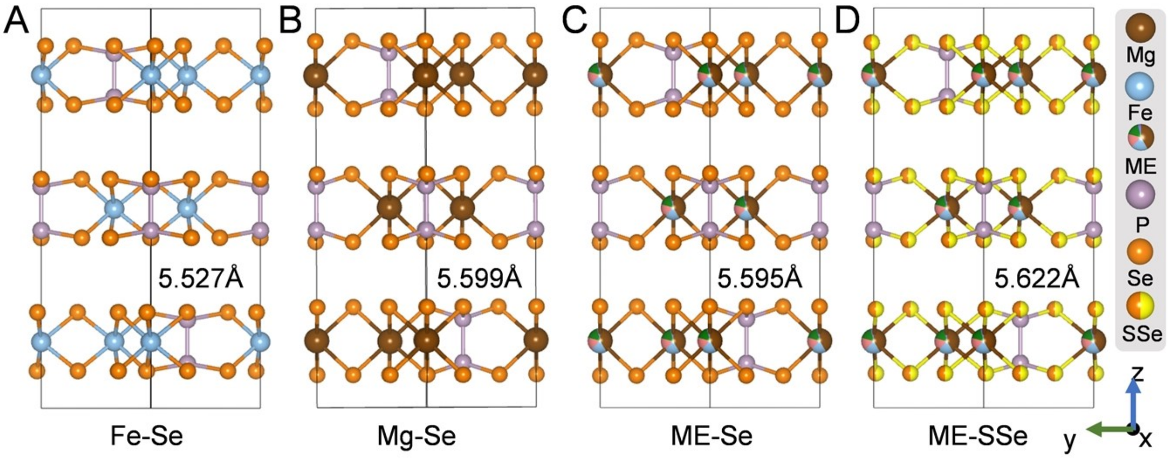

Fig. S2. Front view of the geometry optimized (A) Fe-Se, (B) Mg-Se, (C) ME-Se and (D) ME-SSe models.

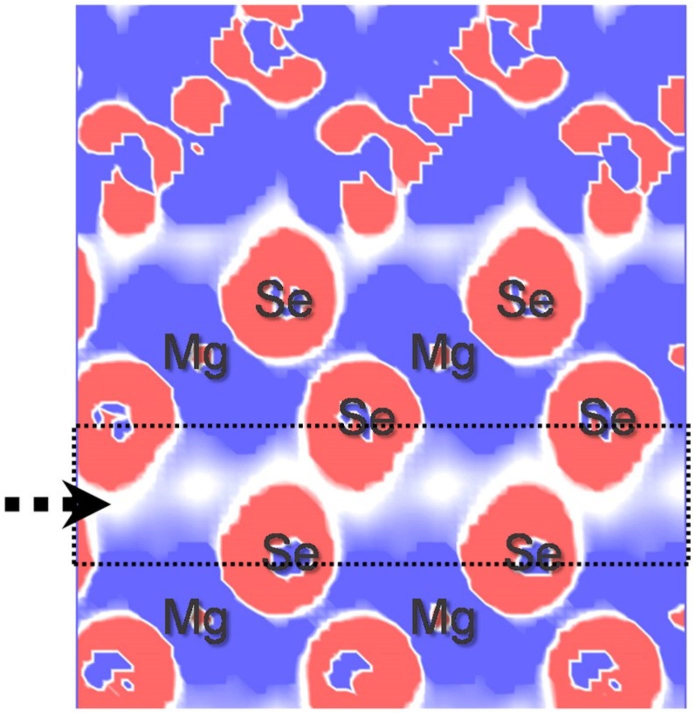

Fig. S3. The electron density difference of Mg-Se model. Electron gain is indicated by yellow at the isosurface of 0.015 |e|/Å^3 and loss by blue at the isosurface of -0.015 |e|/Å^3, while the white part is at the isosurface of 0 |e|/Å^3.

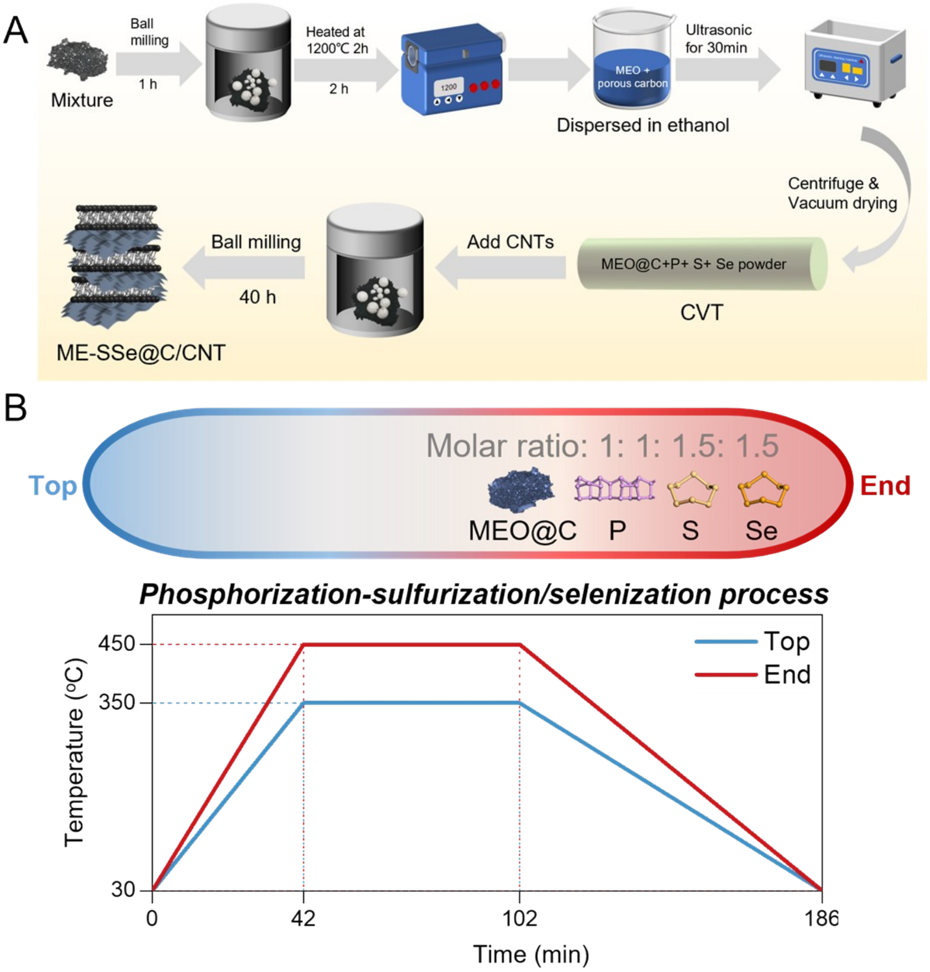

Fig. S4. (A) Schematic illustration of the synthetic process of ME-SSe@C/CNT composite. (B) The heating process to synthesize ME-SSe@C products upon the phosphorization-sulfurization/selenization process.

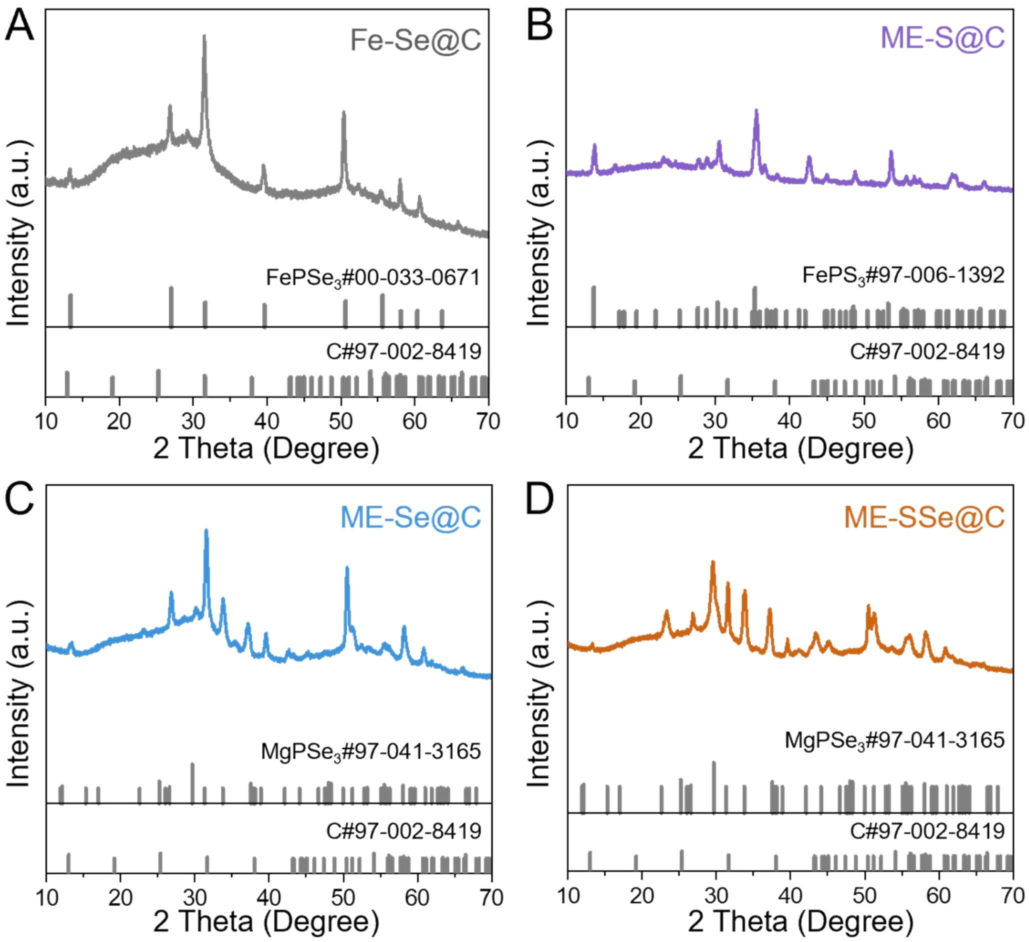

Fig. S5. XRD patterns of (A) Fe-Se@C composite and standard $FePSe_3$ (JCPDS 00-033-0671), (B) ME-S@C composite and standard $FePS_3$ (JCPDS 97-006-1392), (C) ME-Se@C composite and standard $MgPSe_3$ (JCPDS 97-041-3165), and (D) ME-SSe@C composite and standard $MgPSe_3$ (JCPDS 97-041-3165).

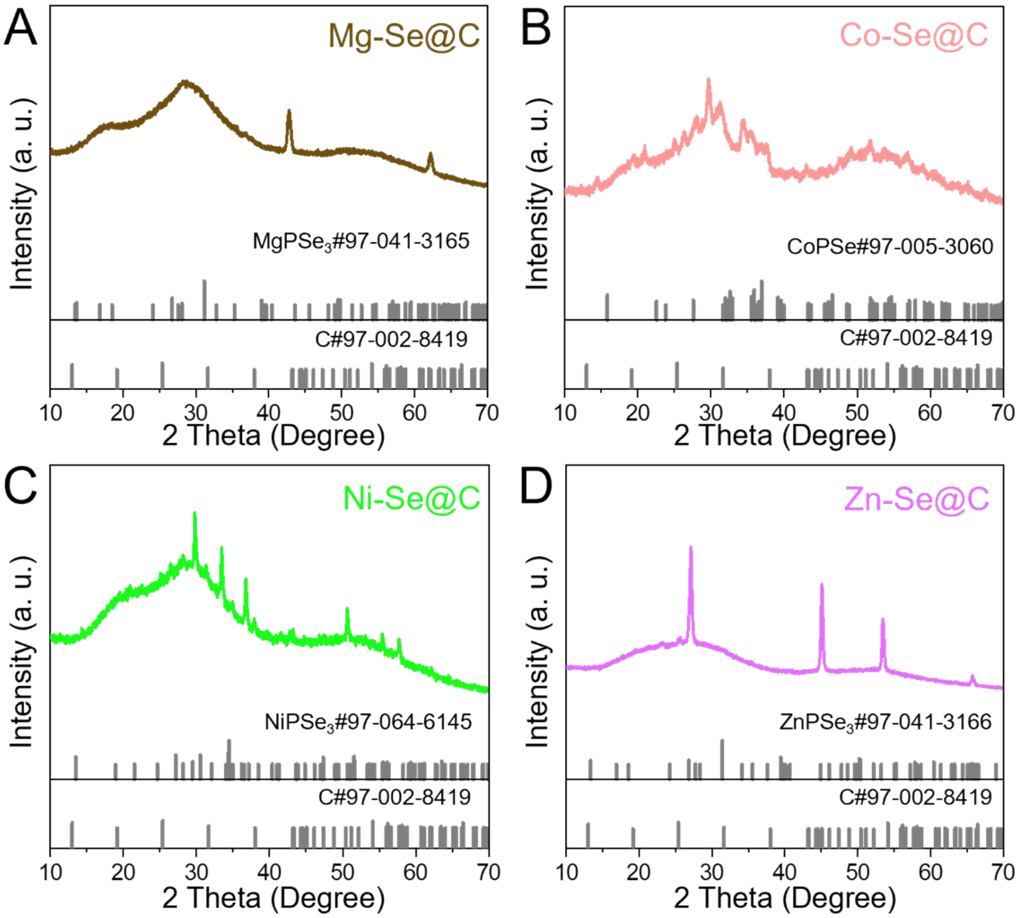

Fig. S6. XRD patterns of (A) Mg-Se@C composite and standard $MgPSe_3$ (JCPDS 97-041-3165), (B) Co-Se@C composite and standard CoPSe (JCPDS 97-005-3060), (C) Ni-Se@C composite and standard $NiPSe_3$ (JCPDS 97-064-6145), and (D) Zn-Se@C composite and standard $ZnPSe_3$ (JCPDS 97-041-3166).

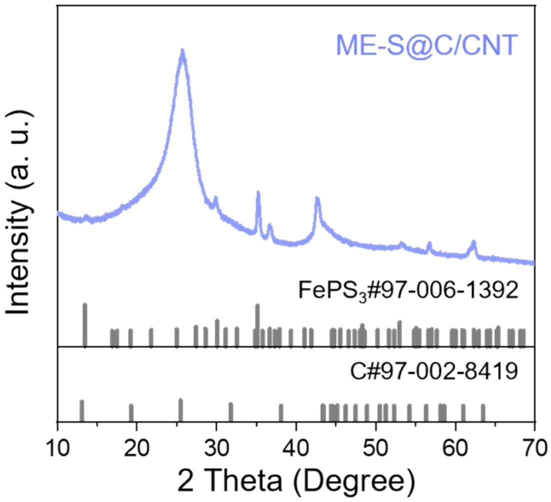

Fig. S7. XRD pattern of ME-S@C/CNT and $FePS_3$ (JCPDS 97-006-1392).

Table S1. The ICP data of three samples.

	Atomic ratio				
Sample	Mg	Fe	Co	Ni	Zn
ME-SSe@C/CNT	0.41	0.19	0.15	0.14	0.11
ME-Se@C/CNT	0.40	0.20	0.15	0.14	0.11
ME-S@C/CNT	0.37	0.20	0.16	0.16	0.10

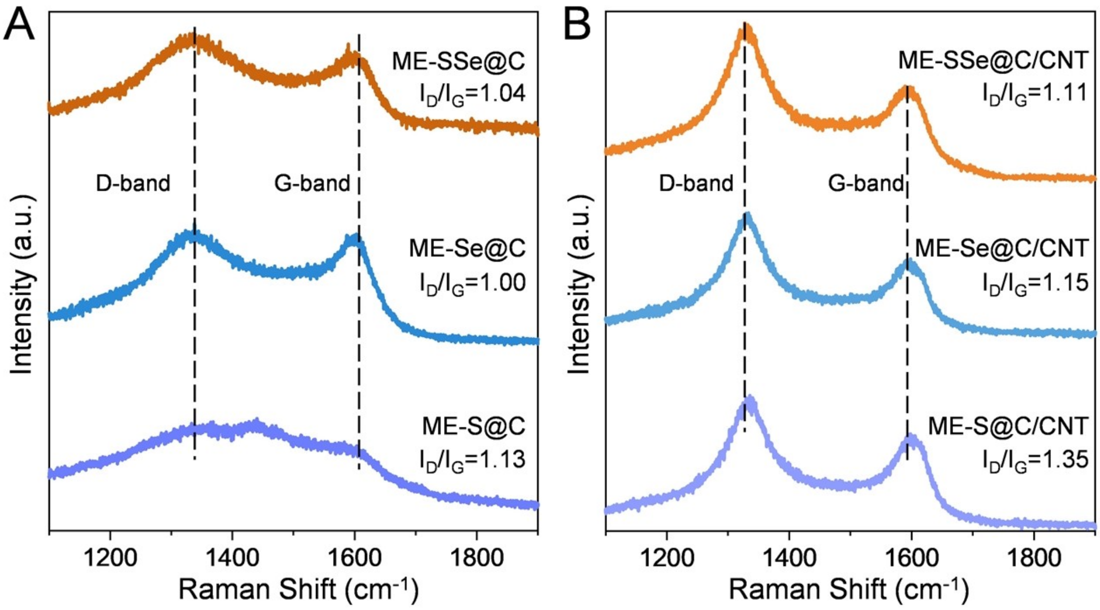

Fig. S8. Raman spectra of (A) ME-SSe@C, ME-Se@C and ME-S@C composite and (B) ME-SSe@C/CNT, ME-Se@C/CNT and ME-S@C/CNT composites.

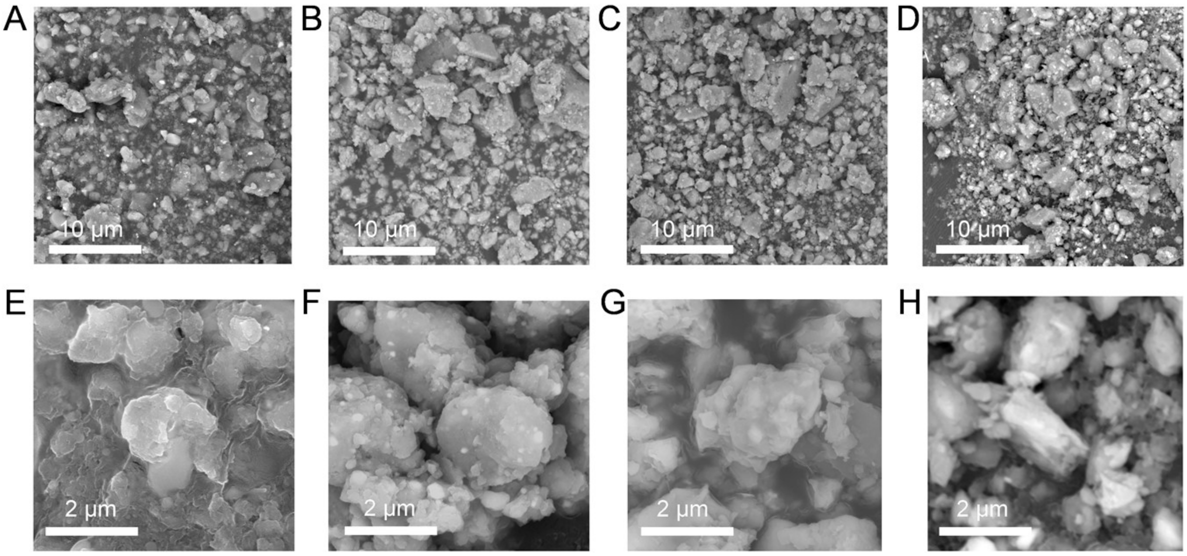

Fig. S9. SEM images for: (A, E) ME-S@C/CNT, (B, F) ME-Se@C/CNT, (C, G) ME-SSe@C/CNT, and (D, H) Fe-Se@C/CNT composites.

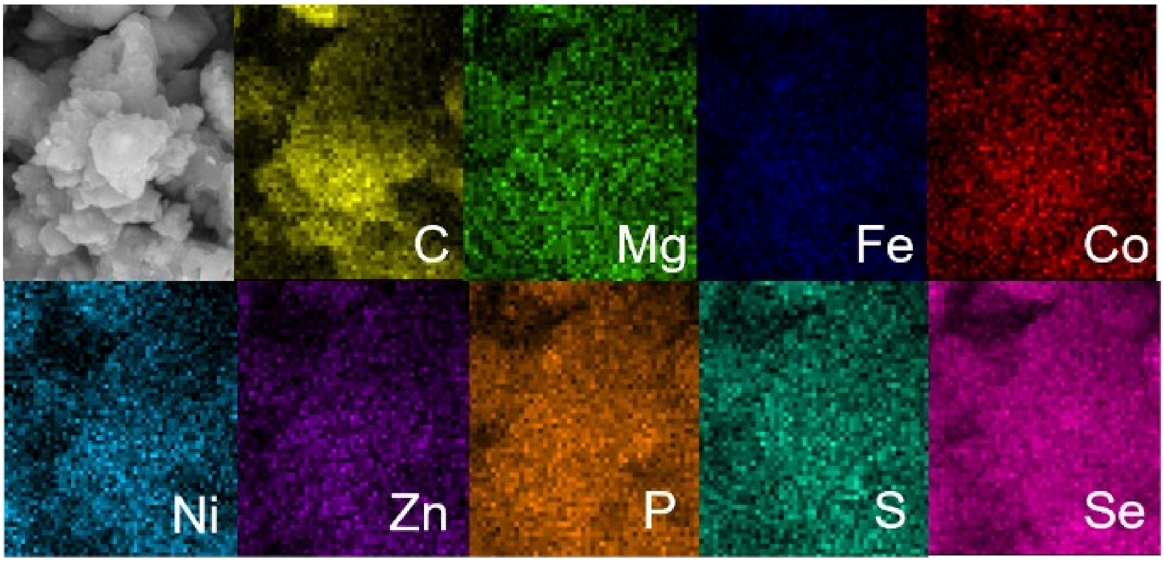

Fig. S10. SEM-EDS mapping images of ME-SSe@C/CNT.

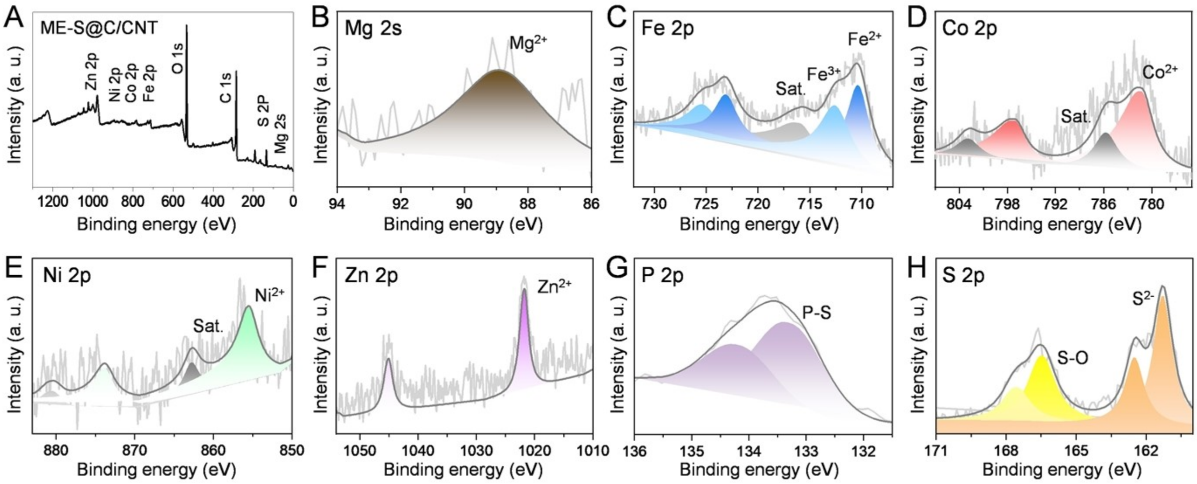

Fig. S11. XPS data of ME-S@C/CNT composite.

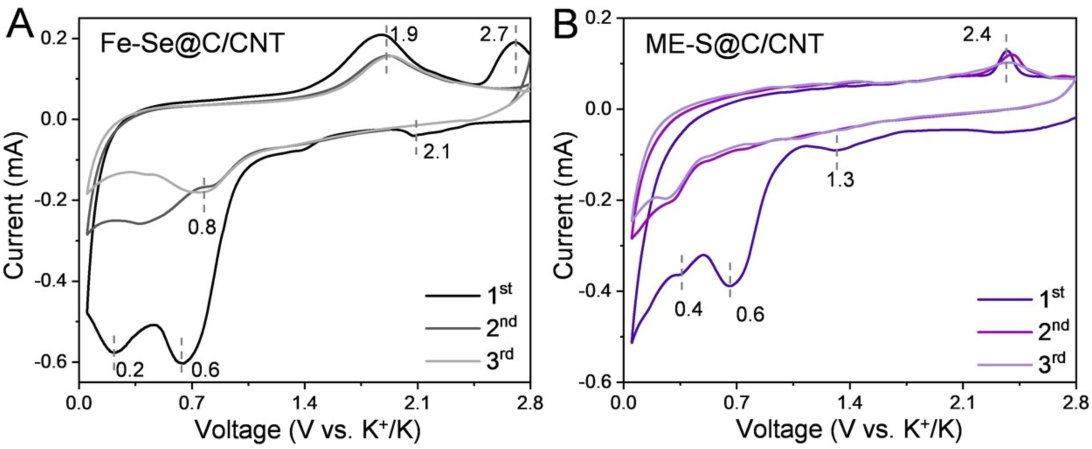

Fig. S12. CV curves of (A) Fe-Se@C/CNT and (B) ME-S@C/CNT at 0.2 mV/s.

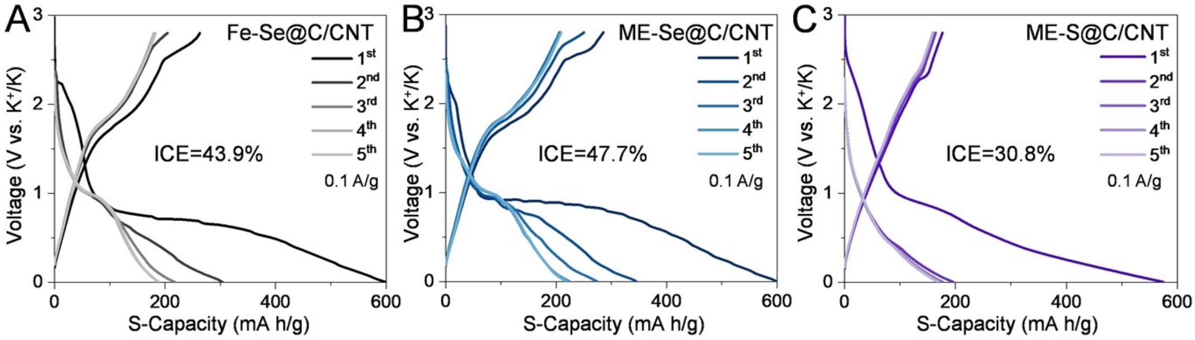

Fig. S13. GDC curves of (A) Fe-Se@C/CNT, (B) ME-Se@C/CNT, and (C) ME-S@C/CNT electrodes at 0.1 A/g.

Table S2. Comprehensive performance comparison of the ME-SSe@C/CNT electrode and other reported related anodes for PIBs.

Materials	Electrochemical performance			References
	Current density (A/g)	Cycle number	Specific capacity (mA h/g)	
ME-SSe@C/CNT	**0.1**	**100**	**232**	**This work**
	0.5	**500**	**148**	
	1.0	**1000**	**124**	
CoP@NPC	0.05	200	162.7	[4]
FeP@CNBs	0.1	300	205	[5]
CoP@C	1.0	400	91	[6]
MoS_2@SnO_2@C	0.05	25	312	[7]
ZnSe@NC	0.1	100	188	[8]
WS_2	0.5	400	48	[9]
$CoS_2/CuCo_2S_4$@NCS	1.0	1000	112	[10]
NPCP@$MoSe_2$	0.5	800	128	[11]
α-MnSe@NC@graphene	1.0	700	92.6	[12]
$MnPSe_3$/Graphite	0.25	700	236.7	[13]
$HEPS_3$@G	0.5	1000	340	[14]

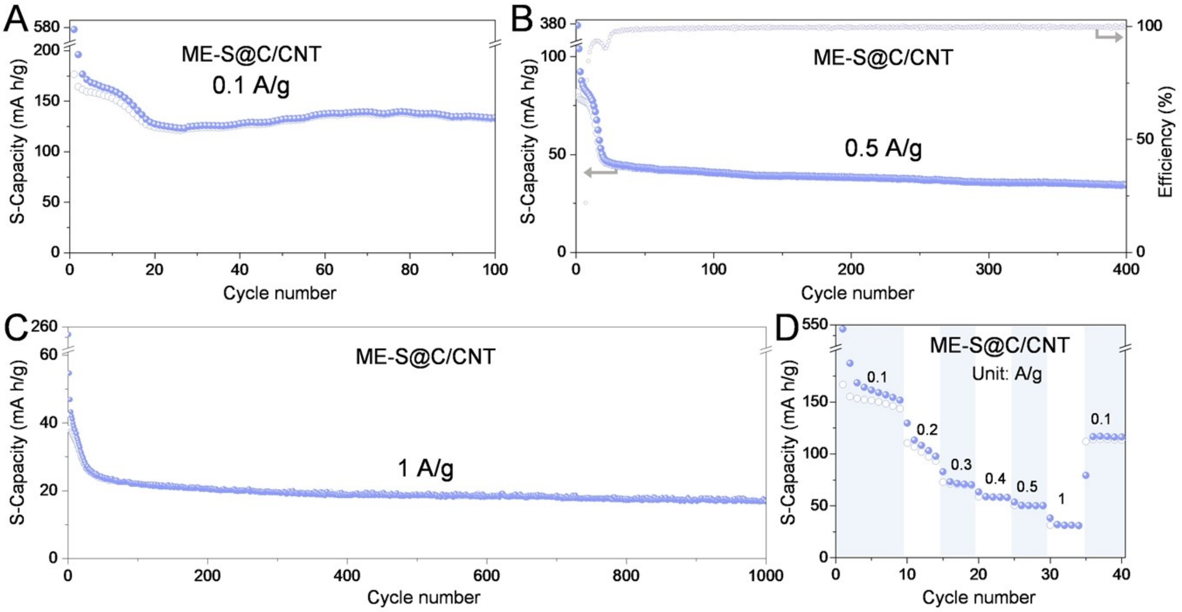

Fig. S14. The cycling performance at (A) 0.1 A/g, (B) 0.5 A/g, (C) 1.0 A/g, and (D) rate capability under various current densities of the ME-S@C/CNT electrode.

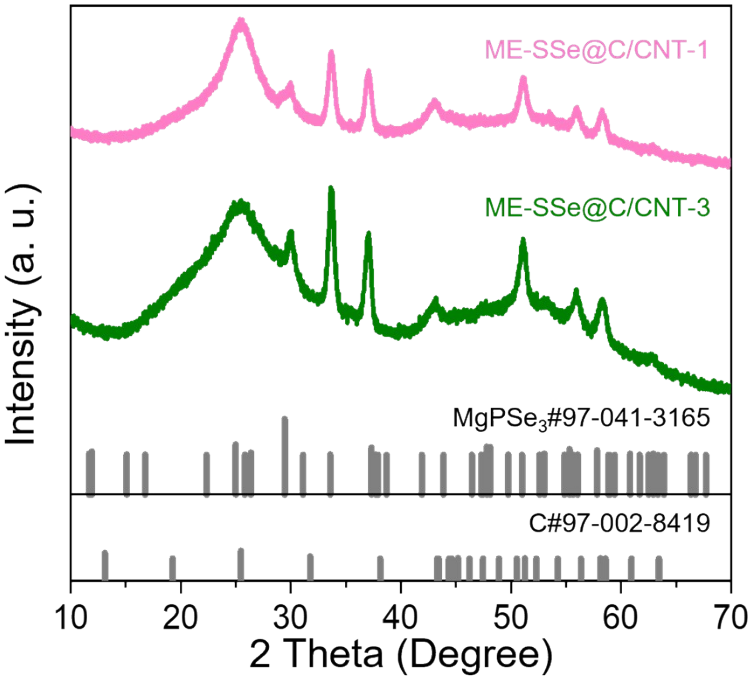

Fig. S15. XRD patterns of ME-SSe@C/CNT-1 and ME-SSe@C/CNT-3 composite.

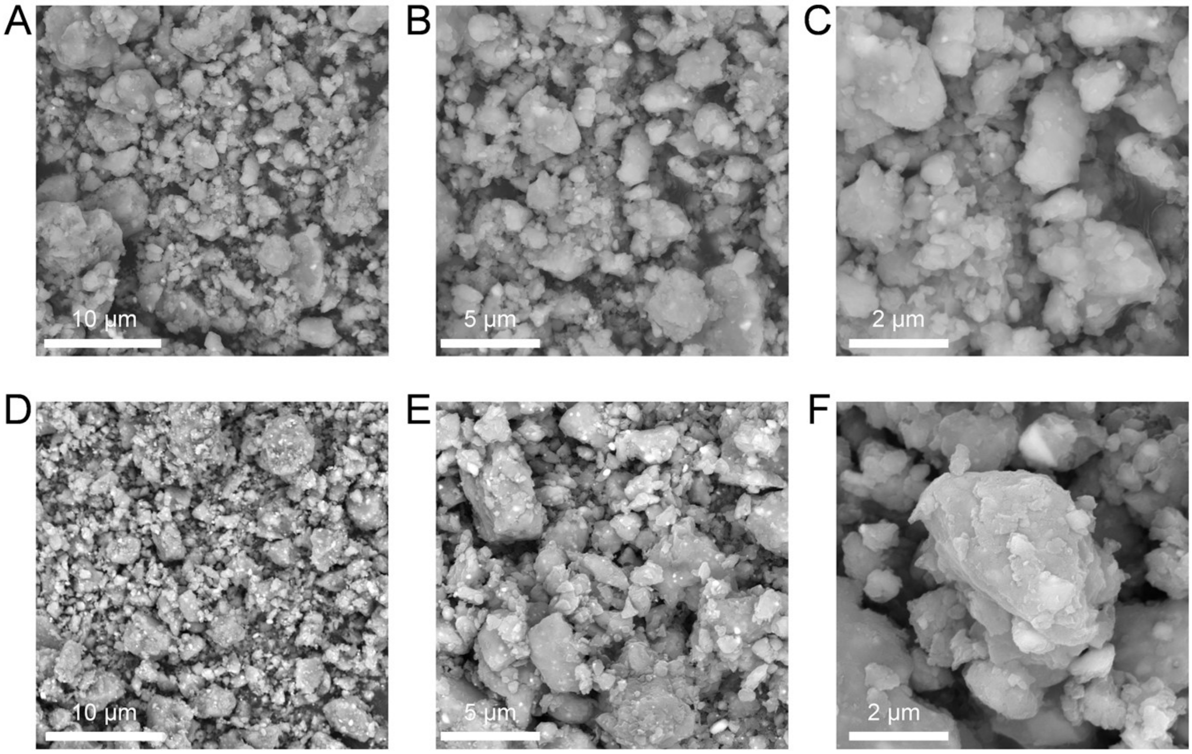

Fig. S16. SEM images of (A-C) ME-SSe@C/CNT-3 and (D-F) ME-SSe@C/CNT-1.

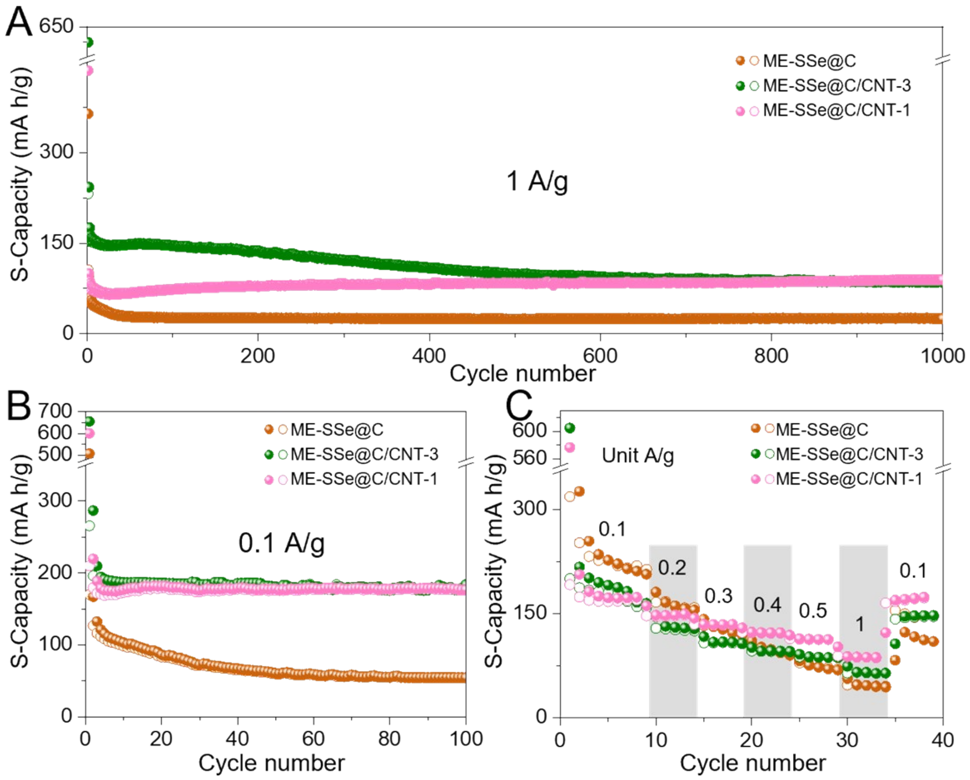

Fig. S17. Cycling performance at (A) 1 A/g and (B) 0.1 A/g, as well as (C) rate capability of the ME-SSe@C, ME-SSe@C/CNT-3 and ME-SSe@C/CNT-1 electrodes.

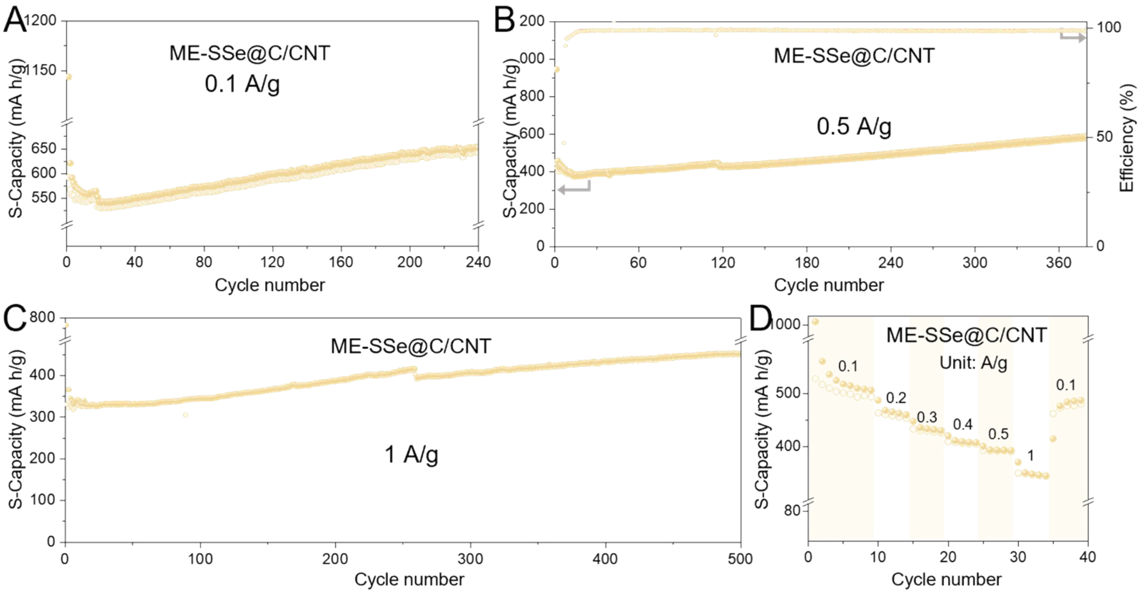

Fig. S18. Cycling performance at (A) 0.1 A/g, (B) 0.5 A/g and (C) 1 A/g, as well as (D) rate capability of the ME-SSe@C/CNT anode for LIBs.

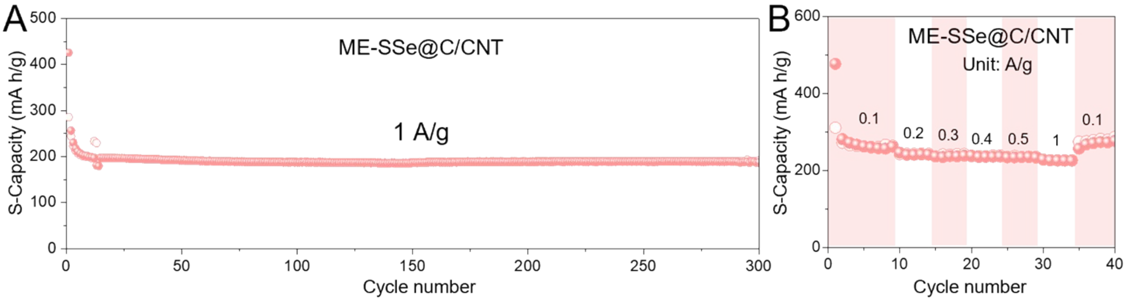

Fig. S19. Cycling performance at (A) 1 A/g, as well as (B) rate capability of the ME-SSe@C/CNT anode for SIBs.

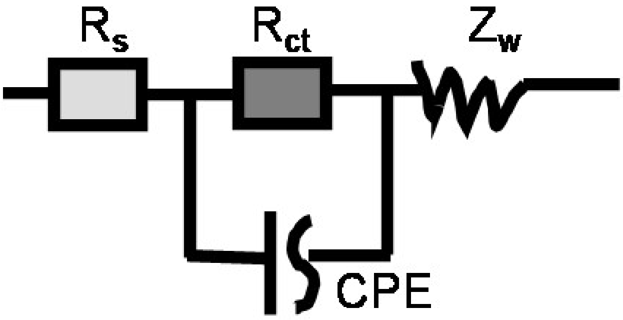

Fig. S20. The equivalent circuit model for the EIS spectra of the ME-Se@C/CNT and ME-SSe@C/CNT electrodes.

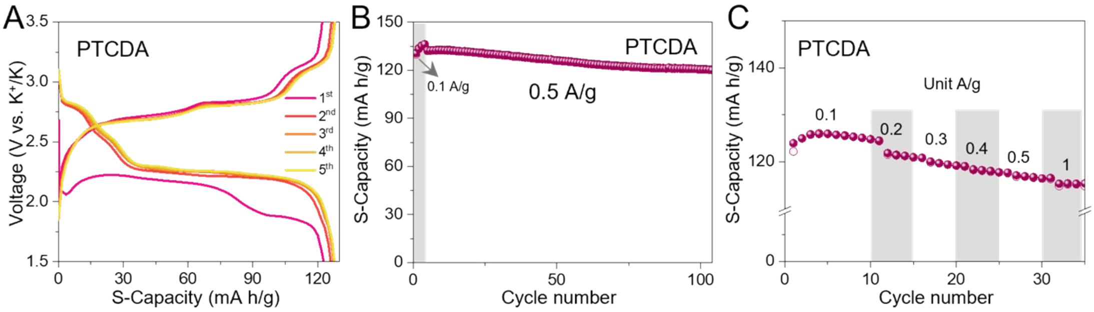

Fig. S21. (A) GDC curves of PTCDA cathode at 0.1 A/g (1.5-3.5 V). The cycling performance at (B) 0.5 A/g, and (C) rate capability under various current densities of the PTCDA material for PIBs.

References:

1 X. Yang and A. L. Rogach, *Advanced Energy Materials*, 2019, **9**, 1900747.

2 J. P. Perdew, K. Burke and M. Ernzerhof, *Physical Review Letters*, 1996, **77**, 3865.

3 S. Grimme, J. Antony, S. Ehrlich and H. Krieg, *The Journal of Chemical Physics*, 2010, **132**, 154104.

4 D. Zhou, J. Yi, X. Zhao, J. Yang, H. Lu and L.-Z. Fan, *Chemical Engineering Journal*, 2021, **413**, 127508.

5 F. Yang, H. Gao, J. Hao, S. Zhang, P. Li, Y. Liu, J. Chen and Z. Guo, *Advanced Functional Materials*, 2019, **29**, 1808291.

6 Q. Liu, Z. Hu, Y. Liang, L. Li, C. Zou, H. Jin, S. Wang, H. Lu, Q. Gu, S. L. Chou, Y. Liu and S. X. Dou, *Angewandte Chemie International Edition*, 2020, **59**, 5159-5164.

7 Z. Chen, D. Yin and M. Zhang, *Small*, 2018, **14**, 1703818.

8 C. Dong, L. Wu, Y. He, Y. Zhou, X. Sun, W. Du, X. Sun, L. Xu and F. Jiang, *Small*, 2020, **16**, 2004580.

9 Y. Wu, Y. Xu, Y. Li, P. Lyu, J. Wen, C. Zhang, M. Zhou, Y. Fang, H. Zhao, U. Kaiser and Y. Lei, *Nano Research*, 2019, **12**, 2997-3002.

10 G. Suo, S. Musab Ahmed, Y. Cheng, J. Zhang, Z. Li, X. Hou, Y. Yang, X. Ye, L. Feng, L. Zhang and Q. Yu, *Journal of Colloid and Interface Science*, 2022, **608**, 275-283.

11 Q. Jiang, L. Wang, Y. Wang, M. Qin, R. Wu, Z. Huang, H. J. Yang, Y. Li, T. Zhou and J. Hu, *Journal of Colloid and Interface Science*, 2021, **600**, 430-439.

12 T. Li, Y. Wang, L. Yuan, Q. Zhou, S. Qiao, Z. Liu and S. Chong, *Chemical Engineering Journal*, 2022, **446**.

13 Y.-F. Huang, Y.-C. Yang, Y.-Y. Tseng and H.-Y. Tuan, *Journal of Colloid and Interface Science*, 2023, **635**, 336-347.

14 P.-W. Chien, C.-B. Chang and H.-Y. Tuan, *Energy Storage Materials*, 2023, **61**, 102853.